Optics and Lasers in Engineering 195 (2025) 109279

Contents lists available at ScienceDirect

Optics and Lasers in Engineering

journal homepage: www.elsevier.com/locate/optlaseng

Modeling a metalens-based system for GHz fiber mode-locked lasers

David M.G. de la Sacristana [a,b,c,*], Luigi Ranno [c], Hung-I Lin [c], Fan Yang [c], Mario Cortijo [a,b], Javier Martí [a,b], Tian Gu [c], Carlos García-Meca [d], Juejun Hu [c]

[a] DAS Photonics, Valencia, Spain
[b] Universitat Politècnica de València, Valencia, Spain
[c] Department of Materials Science and Engineering, Massachusetts Institute of Technology, Cambridge, MA, USA
[d] Monodon, Navantia, Madrid, Spain

ARTICLE INFO

Keywords:
Mode-locked lasers
Fiber optics
Metalens
Polarization control
Saturable absorber
Free spectral range
Two-photon polymerization
Fiber-tip collimator

ABSTRACT

Fiber-based passive mode-locked lasers (MLLs) are a well-established technology for high-speed optical communications, capable of generating ultrashort pulses with high energy. While most commercial MLLs operate at repetition rates around 100 MHz, increasing this frequency to the GHz range introduces significant challenges, including polarization control, efficient saturation of the saturable absorber, heat dissipation and the achievement of a high free spectral range (FSR). To address these limitations, we propose a system consisting of a metalens and a 3D-printed fiber-tip collimator. The metalens is designed to selectively focus one polarization while diverging the orthogonal component, thereby addressing the polarization control. To enhance its performance and increase tolerance to positional offsets and angular tilts, we fabricated a fiber-tip collimator using two-photon polymerization (TPP). Our model suggests that this integrated system could enable the miniaturization of fiber-based MLLs while controlling polarization, enhancing the efficiency of the saturable absorber through better heat dissipation, and increasing the FSR with a shorter fiber length.

1. Introduction

In recent years, the field of nanophotonics has seen significant advances, particularly in the development of metasurfaces which manipulate light with subwavelength structures [1–3]. These innovations offer compact and efficient alternatives to traditional optical components. Metasurfaces, consisting of arrays of subwavelength scatterers, can impart spatially varying phase, polarization, or amplitude responses to incoming wavefronts, effectively replicating and integrating functionalities of conventional optical elements such as lenses [4,5], beam deflectors [6,7] or polarizers [8]. A particularly promising area of application for metasurfaces is in performance enhancement of mode-locked laser systems, which are essential tools in ultrafast optics providing pulses of light with durations in the femtosecond to picosecond range [9,10].

Mode-locked lasers are critical in various scientific and industrial applications, including precision metrology [11], medical imaging [12], and materials processing [13]. The integration of metasurfaces into these laser systems can offer significant advantages, such as compactness, reduced complexity, and enhanced performance. Metasurfaces can replace or augment traditional optical components like mirrors, polarizers, and lenses within the laser cavity, leading to improved control over the laser beam properties and more efficient pulse generation.

Fiber passive mode-locked lasers typically use an erbium-doped fiber (EDF) as the gain medium, which, once pumped, emits light at communication wavelengths and initiates the pulsing mechanism [14–16]. Also critical in a mode-locked laser is the saturable absorber (SA), which initiates and sustains pulsed operation by providing intensity-dependent loss. While various alternative SAs, such as MAX-phase materials, doped fibers, and thin-film composites, have been proposed [17–21], they are generally limited to Q-switching or MHz-range repetition rates and remain incompatible with compact GHz fiber architectures. In this work, we use SESAMs (semiconductor saturable absorber mirrors) from BATOP GmbH, which are specifically designed for GHz operation. Their use has been validated in previous GHz-repetition-rate mode-locked systems [22–25], confirming their suitability for integration in high-speed, passively mode-locked fiber lasers.

However, polarization rotation of light within the cavity and failure to saturate the semiconductor saturable absorber mirror (SESAM) to

* Corresponding author.
E-mail address: dmorgal@doctor.upv.es (D.M.G. de la Sacristana).

https://doi.org/10.1016/j.optlaseng.2025.109279
Received 15 April 2025; Received in revised form 14 July 2025; Accepted 14 August 2025
Available online 22 August 2025
0143-8166/© 2025 The Authors. Published by Elsevier Ltd. This is an open access article under the CC BY-NC license (http://creativecommons.org/licenses/by-nc/4.0/).

initiate the pulsing mechanism are issues that need to be addressed. Polarization rotation within the cavity leads to frequency sidebands, which deteriorates the pulse quality, energy efficiency, peak power and the stability of the laser. These sidebands originate from the formation of polarization-rotating vector solitons, which induce spectral interference and dispersive-wave-like coupling within the cavity [26,27]. This can be compensated by introducing a polarization filter inside the cavity, which resets the polarization state each roundtrip. However, traditional bulky polarizers, such as Glan–Taylor or polarizing beam splitters (PBS)-based elements, pose an integration challenge for lasers operating at high repetition frequencies (above 1 GHz), where the cavity length is small. In addition, a conventional filter is bulky and introduces losses inside the cavity [28].

On the other hand, to saturate the SESAM more rapidly with a short cavity length (high-frequency, long-duration pulses), the fiber and SESAM must be in close proximity to minimize the effective beam area and maximize power density. However, this approach often reduces system durability, as the SESAM can burn out from direct contact during pulsing.

To overcome these challenges, we seek an approach to simultaneously decrease the effective incidence beam area on the SESAM and suppress polarization rotation. To this end, we propose a system combining a 3D-printed collimator lens on the fiber tip and a metalens to selectively focus light based on polarization. We detail the design methodology, simulations results, fabrication and experimental characterization of the fiber collimator and the polarization-selective metalens. The proposed full setup integration device is described and simulated with ray tracing software in Section V and the experimental implementation is subject for future studies.

Previous studies have demonstrated the feasibility of integrating metalenses with fiber platforms in the context of optical systems, including laser-based applications. For example, Wang et al. [29] presented a monolithic metalens-fiber configuration for broadband beam shaping, and Yang et al. [30] introduced a photonic crystal fiber metalens capable of compact focusing and imaging. While these works illustrate the potential of metalens integration within laser-related platforms, they do not address the specific requirements of mode-locked operation. In contrast, our approach targets GHz passive mode-locked fiber lasers by combining polarization-selective focusing and effective beam confinement to enhance SESAM saturation and suppress polarization-induced sidebands, advancing the integration of metasurfaces in high-repetition-rate laser architectures.

2. Concept

To establish a reference configuration, we first consider a conventional mode-locked laser system where a continuous-wave pump at 980 nm excites an EDF as a resonant cavity between a 99/1 with a mirror, and a SESAM. This setup is illustrated in Fig. 1(a). The laser output is shown in Fig. 1(b) and (e) in the wavelength and frequency domains, respectively. Fig. 1(b) shows a spectral profile with the typical sech-squared shape associated with soliton pulses, confirming the mode-locking operation. On the other hand, Fig. 1e highlights the central spectral component used later to analyze sideband formation. Fig. 1(c) zooms into the critical cavity region between the fiber and SESAM, where our optimization will take place. Typically, the approach involves placing the fiber in direct contact with the SESAM to maximize cavity flux and achieve earlier saturation as shown in Fig. 1(c). However, this direct contact leads to heat accumulation in the SESAM, causing burn spots as illustrated in Fig. 1(d). Since the SESAM dissipates optical energy as heat, direct contact with the fiber hinders thermal dissipation, ultimately reducing the lifetime of the system.

Additionally, increasing the PRF requires higher pump power and a shorter active fiber length. As a result, the residual pump power that affects the butt-coupled SESAM increases because of the reduced absorption by the active fiber. This raises the fiber core temperature, further transferring heat to the SESAM.

In conventional methods, to maintain fiber-SESAM alignment, the

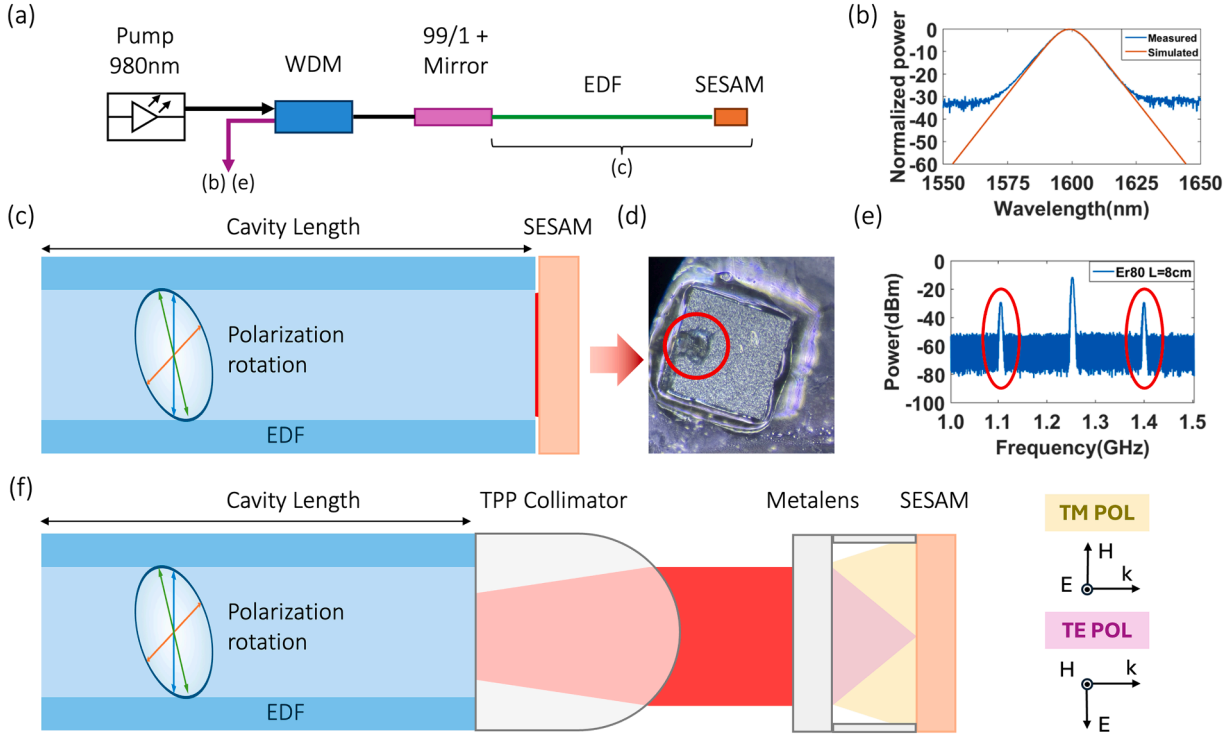

Fig. 1. (a) Fiber-based passive mode-locked laser setup. (b) Simulation (red) and experimental (blue) results of the soliton mode of the mode locked laser with $sech^2$ shape. (c) Schematic of an EDF fiber passive mode-locked laser (PMLL) termination. (d) Burning spot observed in the SESAM. (e) Side bands caused by polarization rotation inside of the cavity. (f) Design proposed in this work to simultaneously control polarization and focus light, which reduces the effective beam area on the SESAM and suppresses side bands. This approach allows for a shorter cavity length, resulting in a higher repetition frequency as demonstrated by Equations (1) and 2.

SESAM is sandwiched between two zirconia ferrules [31,32]. However, the low thermal conductivity of zirconia restricts heat dissipation. Introducing a small gap between the SESAM and the fiber allows heat sinks, as seen in BATOP designs, to significantly improve thermal management.

Intracavity polarization rotation causes the polarization to become elliptical instead of linear when incident on the SESAM. As a result, side bands emerge in the main harmonics, as illustrated in Fig. 1(e). Furthermore, when we separate the fiber from the SESAM, the laser light diverges as it exits the fiber. Therefore, the effective incident beam area increases, which reduces the optical power density when reaching the SESAM. That is why to minimize beam spread, SESAM and EDF are often in physical contact with each other, which tend to cause damage due to hot spot formation.

To make a more robust approach, we should keep some distance between the SAM and the fiber. However, this would reduce the cavity flux and therefore we won't be able to saturate the laser as desired.

In order to keep some distance but achieve the cavity flux, we prepare the focusing metalens to reduce the effective area.

The SESAM saturation flux F_{CAV} defined by the equation [33]:

$$F_{CAV} = \frac{P_{AVG}}{f_{REP} A_{EFF}} \tag{1}$$

Where P_{AVG} is the average power inside the cavity, f_{REP} is the repetition frequency of the pulses and A_{EFF} is the effective beam area incident on the SESAM. Clearly, decreasing the effective beam area A_{EFF} increases the SESAM saturation flux, thereby improving the pulsing initiation. Also, we note that the repetition frequency can be defined from the cavity parameters as [33]:

$$f_{REP} = \frac{c}{2 n_{EFF} L_{CAV}} \tag{2}$$

Where c denotes the speed of light in vacuum, n_{EFF} is the effective index of the fiber mode and L_{CAV} the length of the cavity. The factor 2 applies for a linear cavity and vanishes in the case of a circular cavity. Therefore, if f_{REP} increases, L_{CAV} decreases and it becomes more difficult to reach the average power needed to saturate the SESAM with less gain medium.

Introducing a focusing metalens between the fiber and the SESAM allows for more efficient saturation of the SESAM using the same average power and avoiding direct contact. Fig. 1(d) illustrates our system design concept, addressing both polarization control and focusing functions. The collimator lens was printed on the fiber tip using TPP and serves to enhance the system's tolerance to misalignment between the fiber and the metalens. Fiber tip collimators and their applications to fiber lasers have been previously reported in the literature [34–37] although a fiber-tip collimator in a passive mode-locked laser has not yet been demonstrated to address this issue.

The Supplementary Material explores alternative solutions to this challenge, providing a comparative analysis of their respective pros and cons.

3. TPP collimator

The lens collimator was designed using the ZEMAX ray tracing module. Fig. 2(a) and (b) show the design and simulation results. The aspheric lens material is IP-S resin and its optimized design parameters are: a thickness of 158 μm, a radius of −50 μm, a conic constant of −462 μm, and a 4th order term of 0.96 μm. This design results in a lens that collimates light while providing better tolerance to misalignment.

Fig. 2(d) showcases a collimator lens directly printed onto a fiber tip. This was accomplished using a fiber aligner to manually align the tip of the fiber with the stage of a TPP NanoOne printer, as detailed in the experimental section. The inset of Fig. 2(d) reveals the measured beam profile at 130 mm distance from the collimator. In addition to the central collimated spot, a halo is also visible likely due to the diffraction in TPP

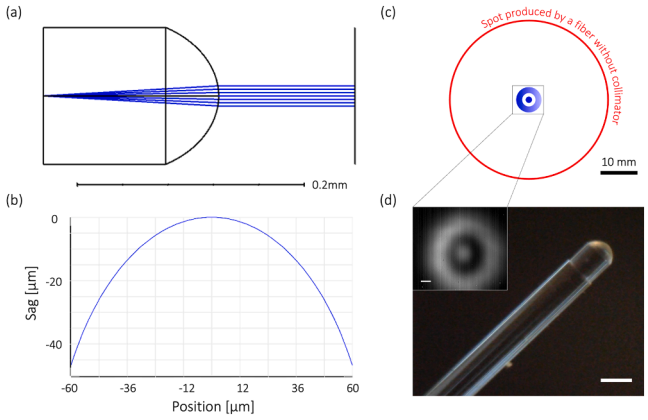

Fig. 2. Design, fabrication and characterization of the TPP collimator. (a) Simulated collimator design in ZEMAX. The radius of the cylinder corresponds to that of a commercial EDF of 60 μm and the height of the pilar is 120 μm. (b) Optimized aspheric lens sagitta. (c) Schematic of the spot produced by the fiber (NA = 0.13) at a distance of 100 mm (outer ring), compared with the experimentally observed collimated spot and the diffraction halo at the same distance (inner ring). (d) Microscope image of the collimator printed on the EDF. The inset displays the experimental result of the collimated spot and the diffraction halo described in (c). Scale bar = 1 mm.

stepping resolution. Improved fabrication accuracy will suppress the halo formation.

Fig. 2(c) shows a comparison of the experimentally measured dimensions of the spot and the theoretically calculated spot of the fiber without the collimator at the given distance. The calculated spot without the collimator has a radius of 21.5 mm. On the other hand, we measure that the halo has an inner radius of 1.8 mm and an outer radius of 3.44 mm while the collimated spot has a radius of 0.9 mm. Despite the presence of the halo effect, the collimator produces a significantly smaller spot size compared to a cleaved fiber, while maintaining the spot dimensions over a long distance. Further investigation and refinement of the manufacturing process are necessary to minimize these halo effects and enhance the overall performance of the collimator.

4. Polarization dependent metalens

Our objective here is to create a lens capable of focusing TE-polarized light and making TM-polarized light diverge, effectively diminishing the power density of the orthogonal polarization. We selected a-Si ($n = 3.54$, thickness = 997 nm) to fabricate the meta-atoms and a substrate of fused silica ($n = 1.443$, thickness = 3 mm) as shown in Fig. 3(a).

These values correspond to the target working wavelength of 1567 nm. Fig. 3(a) shows the geometry of the meta-atom with a pitch equal to 800 nm. The length and width of the meta-atom were parametrized from 100 to 700 nm and the corresponding transmission phase and amplitude are shown in Fig. 3(b) and (c), respectively.

These meta-atom simulations have been performed using RCWA for these parameters. In addition, we computed the phase difference between both polarizations in Fig. 3(d). The result shows that we can cover 0 to 2φ phase difference, which enables phase control between the two polarizations for this focusing-diverging case. The metalens has a radius of 60 μm and a focal length of 220 μm which results in a NA of 0.273. The wrapped hyperbolic target phase profiles for the two orthogonal polarization are shown in Fig. 3(e) for TE polarization and Fig. 3(f) for TM polarization. The focusing phase profile follows the well-known formula $\varphi(x,y) = \frac{2\pi}{\lambda}\left(\sqrt{f^2 + x^2 + y^2} - f\right)$, with λ being the designed wavelength, f the focal length and x,y the metalens inplane coordinates. The diverging phase profile adds a minus sign. The left halves of the plots represent the target phase profile while the right halves indicate the

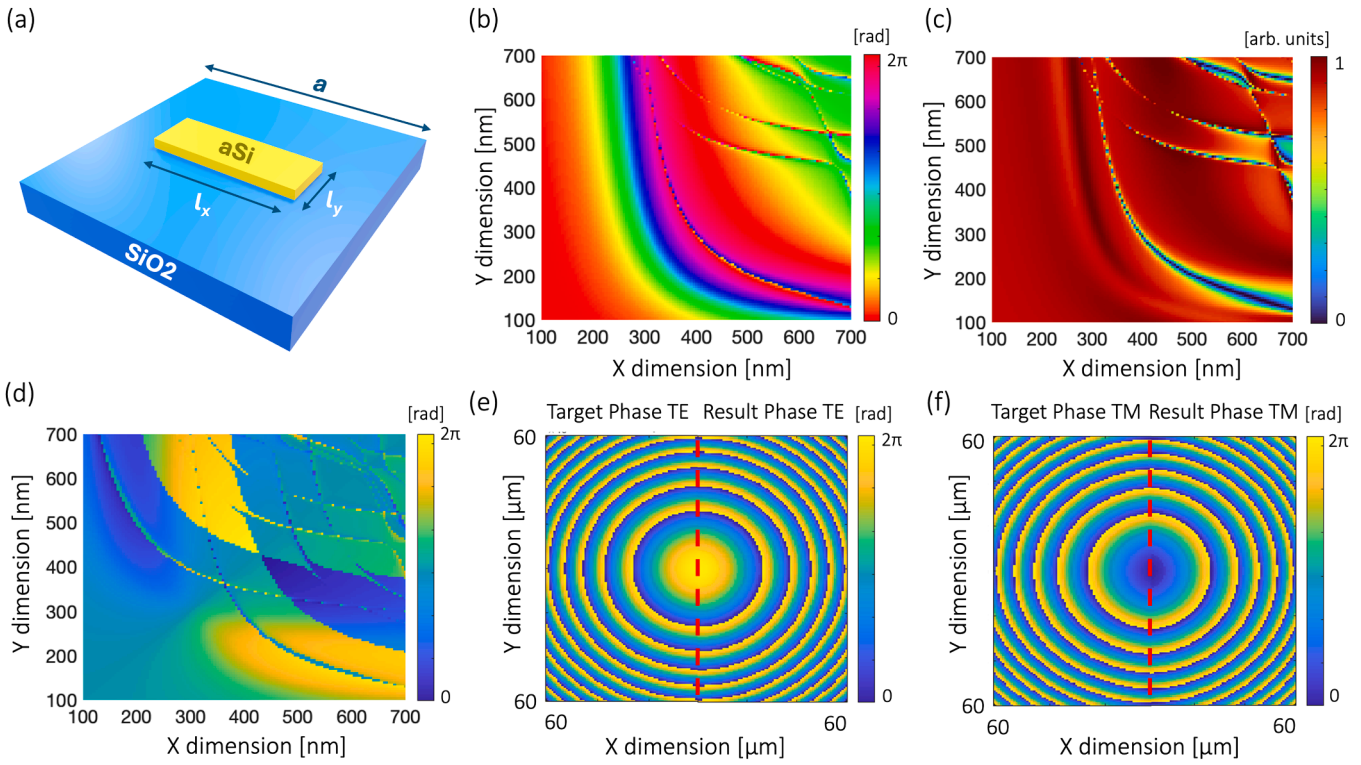

Fig. 3. Design of the polarization-dependent metalens. (a) Meta-atom configuration with fused silica as the substrate and a-Si as the meta-atom material. The dimensions l_x and l_y represent the lateral size of the meta-atom. (b) Parameter sweep of the phase response of the meta-atom for a range of 100–700 nm for l_x and l_y for TE polarization. (c) Parameter sweep of the amplitude response of the meta-atom for a range of 100–700 nm for l_x and l_y for TE polarization. (d) Phase difference between two orthogonal polarizations (TE and TM). (e) Target phase profile for TE polarization aimed at focusing the light. (f) Target phase profile for TM polarization aimed at diverging the light. In figures (e) and (f), the left halves show the target phase profile, while the right halves display the simulated result with the selected meta-atoms.

phase profile obtained with the simulated meta-atom responses. Our design follows the approach discussed in [38], which defines a figure-of-merit as follows:

$$FOM_{TE} = T_{avg,TE}\left(\frac{sin\ (2\langle|\phi_{meta,TE} - \phi_{target,TE}|\rangle}{2\langle|\phi_{meta,TE} - \phi_{target,TE}|\rangle}\right)^2 \tag{3}$$

$$FOM_{TM} = T_{avg,TM}\left(\frac{sin\ (2\langle|\phi_{meta,TM} - \phi_{target,TM}|\rangle}{2\langle|\phi_{meta,TM} - \phi_{target,TM}|\rangle}\right)^2 \tag{4}$$

$$FOM_{EFF} = \sqrt{FOM_{TE} \cdot FOM_{TM}} \tag{5}$$

Where the target phase profiles are represented by $\phi_{(\text{target,TM})}$ and $\phi_{(\text{target,TE})}$, and the simulated phase profiles based on the meta-atom selections are indicated as $\phi_{(\text{meta,TM})}$ and $\phi_{(\text{meta,TE})}$. Meta-atoms that maximize FOM_{eff} were chosen in our design.

Fig. 4 presents simulations showing light propagation through the metalens for TM and TE polarizations. These results were derived using the Kirchhoff diffraction integral applied to the respective phase profiles [39]. The diverging behavior for the TM polarization is clearly observed in Fig. 4(a), (c) and (d).

Conversely, for the TE polarization (Fig. 4(b) and (c)), a pronounced focusing effect is observed, with significant power concentration at the focal spot. For this polarization, the lens exhibits a focusing efficiency ($\eta = \frac{I_{5FWHM}}{I_{incident}}$) of 0.931, where I_{5FWHM} represents the sum of the intensity within a region equal to five times the full width at half maximum (FWHM), and I_{incident} denotes the total incident intensity summed over the entire lens width. In the focusing case, the FWHM is 1.6 μm so the sum intensity calculated for the efficiency is performed over a spatial width of 8 μm. With focusing, the effective beam area in the SESAM (A_{EFF}) is significantly reduced by the metalens. Without the metalens, the beam exiting the fiber (numerical aperture NA = 0.13) diverges over the 220 μm distance to the SESAM, resulting in an approximate spot radius of 28.8 μm and an effective area of $A_{EFF,1} = 2.61 \times 10^{-9}$ m^2. With the metalens (NA = 0.273), the diffraction-limited spot radius is reduced to approximately 3.2 μm (see Fig. 4(c)), yielding $A_{EFF,2} = 3.85 \times 10^{-11}$ m^2. This corresponds to a reduction factor of approximately 68.

Since the SESAM saturation fluence (F_{SAT}) is inversely proportional to A_{EFF}, this reduction dramatically increases by 68 times the incident power density at the SESAM surface, enabling more efficient and faster saturation. For a given average intracavity power, this enhancement lowers the threshold for mode-locking and contributes to maintaining stable operation even at GHz repetition rates.

In terms of polarization performance, the design yields 16.3 dB contrast between the peak intensities of the TE and TM polarizations on the focal plane, effectively suppressing intra-cavity polarization rotation.

Several studies have demonstrated that improving polarization discrimination within the laser cavity (using intracavity polarizers, polarization-maintaining fiber, or polarization-sensitive nonlinear elements) can substantially suppress spectral sidebands, often by more than 15–20 dB. For instance, Lei et al. [40] employed a fiber-integrated polarization filter to achieve >20 dB suppression of Kelly sidebands in a soliton laser system, while Avazpour et al. [28] demonstrated comparable reduction using a polarization-imbalanced nonlinear loop mirror.

In our case, the metalens achieves a polarization contrast of 16.3 dB, in linear scale corresponding to a suppression ratio of approximately 43:1 for the orthogonal polarization component. This level of polarization selectivity is consistent with thresholds reported in the literature for effective sideband suppression. Unlike conventional polarizing optics,

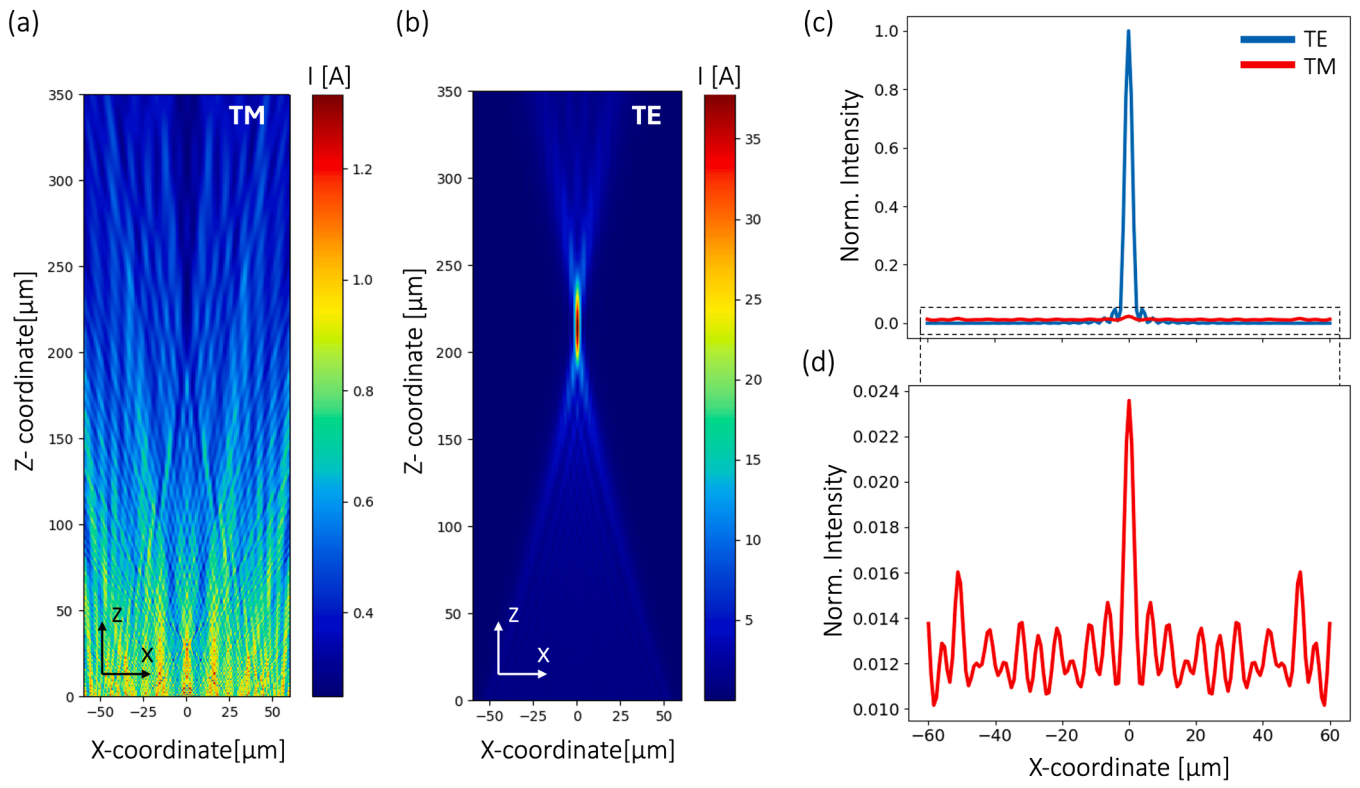

Fig. 4. Simulation results of the metalens. Optical intensity distributions along a longitudinal section for (a) TM and (b) TE polarizations. The metalens is located at $z = 0$. The TE polarized light converges, with a focal length of 220 μm, consistent with our target. Transverse optical intensity distributions on the focal plane for (c) TE and TM polarizations normalized to the maximum amplitude in the TE case. (d) Zoom of the TM case.

the metalens operates entirely in the transmission mode, selectively focusing the desired polarization while scattering the orthogonal component outside the mode volume. This allows for polarization control without introducing reflective feedback or additional insertion loss, features particularly advantageous in compact, high-repetition-rate laser architectures.

Next, the metasurface was fabricated following protocols detailed in the Experimental Section. Fig. 5(a) shows scanning electron microscope (SEM) images of the fabricated metasurfaces. To characterize the metalens, we evaluated the focal spot and divergence for both polarizations with a polarizer placed before the metalens. The measurement setup, illustrated in Fig. 5(b), involved a 1567 nm laser and a collimator mounted on a rail. The focal spot was magnified using a pair of lenses arranged as a telescope assembly and captured with an infrared camera. The focal spot images for both TE and TM polarizations are presented in Fig. 5(c) and (d).

The results show a well-defined focal spot for the TE polarization and apparent beam divergence for the TM polarization, validating the ability

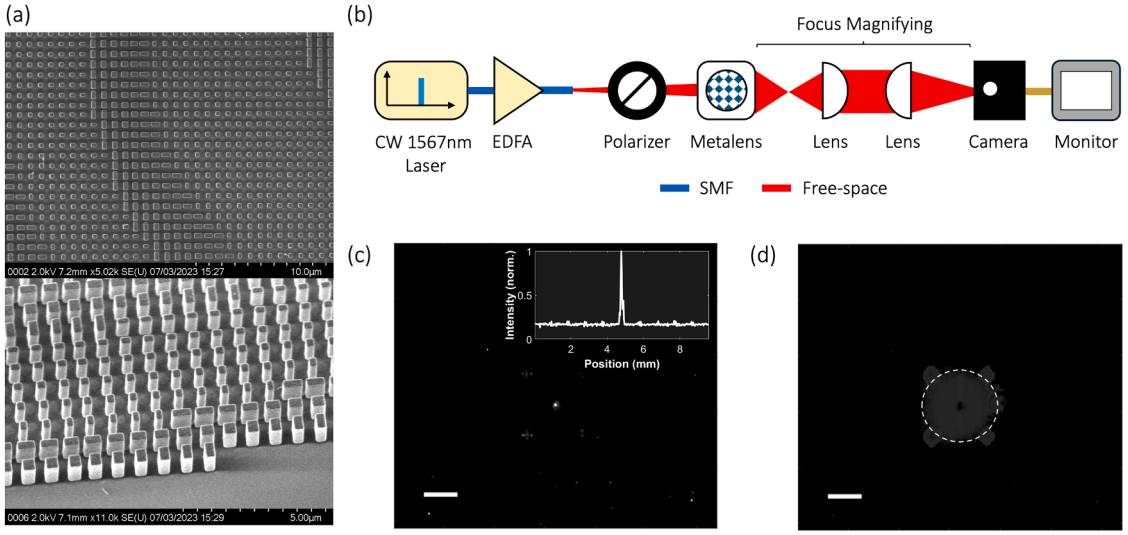

Fig. 5. Fabrication and characterization of the metalens. (a) SEM images of the fabricated metalens. (b) Setup employed to characterize the beam quality. (c-d) Beam profiles captured for (c) TE polarization on the focal plane (inset shows the section of the focusing profile) and (d) TM polarization at the same position (diverged area is encircled). The four spots at the corners are due to light scattering at the alignment marks patterned on the same substrate as the metasurface. Scale bars = 1 mm.

of the metalens to selectively focus light based on polarization.

Notably, due to initial design simplifications, the metalens is optimized for a specific wavelength, while mode-locking is characterized by a broad spectral window. Simulations in Supplementary Material B show that the focusing spot offset remains below 10 μm across a 60 nm wavelength bandwidth, comparable to the MLL bandwidth. While the impact is expected to be minimal, future designs could further enhance achromatic performance.

5. System modeling

To evaluate the performance of the proposed design within a mode-locked aser, we simulated the entire collimator-metalens-SESAM assembly in ZEMAX, as illustrated in Fig. 6. The metalens was implemented as a binary surface using a polynomial approximation of the calculated focusing phase profile. Fig. 6(a) plots the TE polarization focal spot profile on the SESAM in the absence of misalignment. In this simulation, our goal was to assess the tolerance of the system to offset and tilt, defining the limit in a Strehl ratio lower than 0.9. The Strehl ratio is calculated based on the Optical Path Difference (OPD) of the wavefront relative to an ideal diffraction-limited wavefront. The system shows good tolerance in response to transverse offset between the collimator and the metalens as shown in Fig. 6(b) and (e). For instance, under conditions of maximum offset (16 μm, typically < 5 μm in practice), we still observed acceptable ray paths and a slightly distorted spot. Similarly, the effect of tilt is shown in Fig. 6(c) and (f), showing that the system maintains good focusing characteristics even at a tilt angle (8.3°) well beyond the normal operational range (typically $<1°$ for the fiber).

These specifications comfortably exceed the offset and tilt tolerances observed in commercial aligners (e.g.: F-131, PI or FiberPort Aligner, Thorlabs), confirming the practicality of the design for experimental implementation. Such mechanical compatibility is particularly relevant in the context of GHz mode-locked laser systems, where compact cavities amplify sensitivity to misalignment. Unlike their MHz-rate counterparts, where alignment margins are more forgiving due to longer cavities and larger beam sizes, GHz systems generally require micron-scale precision and tight angular control to maintain optical stability [41,42]. As summarized in Table 1, our system achieves tolerance levels typically tighter than those required in MHz systems but more relaxed than those demanded by conventional GHz architectures. This favorable alignment margin, enabled by the printed fiber collimator, enhances the manufacturability and robustness of the laser system without compromising optical performance.

These positive results underscore the important role of the collimator in achieving not only excellent metalens performance but also robust tolerance to potential offsets and tilt in real-world system implementations.

6. Conclusion

In this work, we proposed a system architecture designed to enhance laser saturation time by reducing the effective incidence area through polarization-dependent focusing. By selectively focusing one linear polarization while diverging the orthogonal component, the system also acts as a filter to suppress side lobes. We experimentally characterized the performance of the polarization-dependent metalens and fiber-tip collimator.

Future work will focus on integrating the proposed system into an MLL architecture to further validate the model. This experimental

Table 1
Alignment Tolerances in passive fiber MLLs.

Parameter	Commercial MHz MLLs [43]	GHz MLLs [41]	This work
Tolerance (lateral offset)	Tens to hundreds of micrometers	Typically few micrometers	± 16 μm (Strehl ratio > 0.9)
Tolerance (angular tilt)	Several Degrees	Typically < 5°	± 8.3°
Alignment tool resolution	Manual or coarse	< 1 μm, sub-degree	< 1 μm, < 0.1°

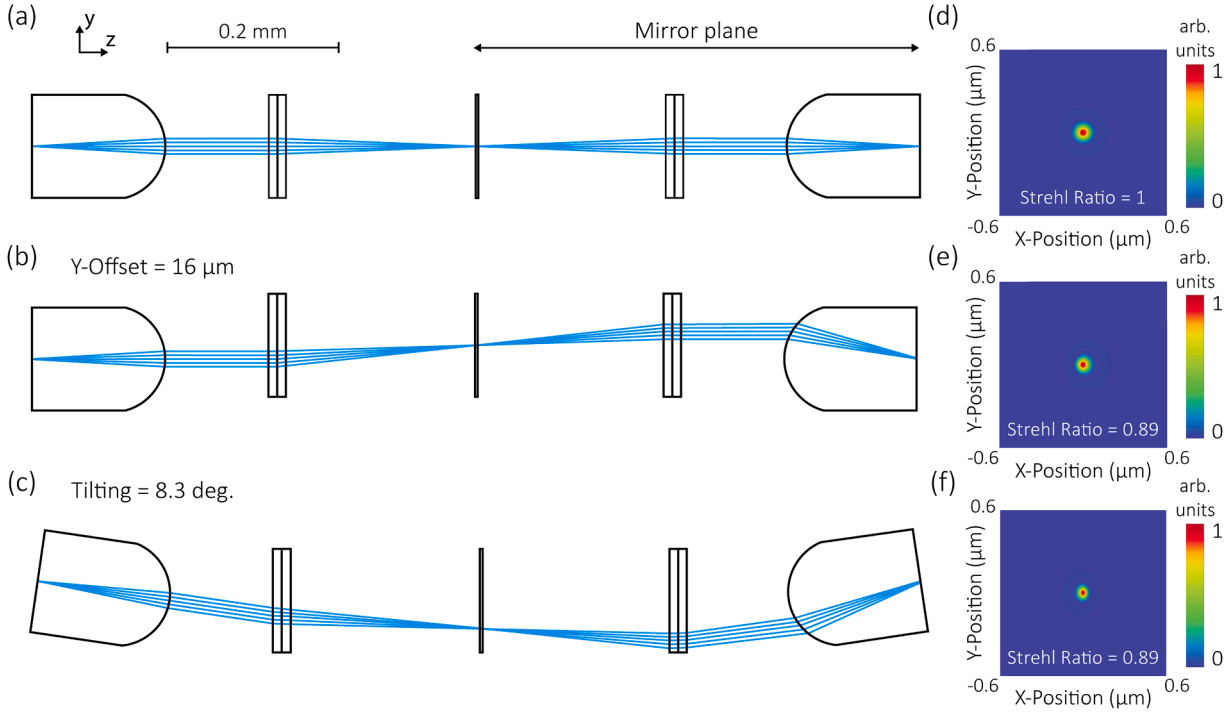

Fig. 6. ZEMAX simulation of the collimator-metalens-SESAM assembly. The mirror-symmetric configuration is used to emulate mirror reflection on the SESAM. Ray trace simulations of the assembly (a) in the absence of misalignment; (b) with 16 μm fiber offset along the transverse direction; and (c) with 8.3° tilt of the collimator lens. (d-f) Simulated TE polarization focal spot profiles on the SESAM corresponding to (a-c).

implementation presents challenges, as it requires precise alignment control and dedicated setup adjustments. However, to anticipate practical constraints, we analyzed the system's tolerance to tilts and offsets, achieving a Strehl ratio above 0.90 in simulations for tilts up to 8.3° and offsets of 16 μm. These results highlight the potential of this architecture to improve the performance of passive mode-locked lasers for high-frequency operation, opening the door to future experimental implementations.

Beyond these specific results, the work presents several broader technical contributions. First, it demonstrates the co-design of a fiber-integrated collimator and a dielectric metalens capable of polarization-selective focusing in a compact and manufacturable form factor. This combination enables both increased power density at the saturable absorber and suppression of polarization-induced sidebands, two key bottlenecks for GHz-range passive mode-locking. Second, we validate through ray-tracing simulations that the proposed system offers substantial tolerance to mechanical misalignments, with performance margins that exceed the resolution capabilities of standard commercial alignment tools. This robustness is critical for enabling scalable and reproducible integration into practical laser systems.

The relevance of this work is further supported by comparison with the state of the art and alternative approach ideas as detailed in the Supplementary Material. Unlike conventional collimation and polarization filtering schemes, which rely on bulk free-space optics with strict alignment demands, our approach provides a flat-optics solution that reduces both footprint and complexity while preserving performance.

While the polarization contrast and effective area reduction were experimentally demonstrated and modeled, full system integration with a functioning mode-locked cavity remains a topic for future investigation. Additionally, direct measurement of spectral sideband suppression and long-term thermal reliability will be important steps in validating real-world performance.

Overall, the results presented here support the feasibility of metasurface-assisted engineering of mode-locked cavities and establish a new design pathway toward compact, robust, and efficient GHz-repetition-rate fiber laser systems.

7. Experimental section

Metalens fabrication: The amorphous Si with 450 nm thick was deposited on a 0.5 mm thick fused silica wafer by plasma-enhanced chemical vapor deposition (STS PECVD). Then, the wafer was diced into square size of 12.5 mm as the metalens substrates. To fabricate the metalens, the electron beam resist (ma-N 2402, Micro Resist Technology) and then a thin layer of conductive polymer (ESpacer 300Z, Showa Denko America, Inc.) were spin-coated on the substrates for electron beam lithography (EBL). The EBL was written at a voltage of 50 kV and a beam current of 1 nA (Elionix HS50). Then, the sample was put in the developer (AZ 726 MIF Developer) to produce the mask patterns and gently rinsed with deionized water. To etch the amorphous Si, the dry-etching was performed by dual plasma sources and dual gas inlets with a mixture of SF6 and C4F8 (SPTS Rapier DRIE). Residual electron beam resist was stripped by O2 plasma ashing. Areas on the substrate not occupied by the metasurface were subsequently covered by a metal mask to prevent stray light. To fabricate the metal mask, photoresist of AZ nLOF 2035 was spin-coated on the metalens at 3000 rpm. The resist was soft baked at 115 °C for 1 min, exposed to UV light on a MLA150 Maskless Aligner, and then post-exposure baked at 115 °C for 1 min. The photoresist was developed by immersing the sample into Microposit MF-319 developer for 1 min and gently rinsed with deionized water. Then, a 200 nm thick Au layer was deposited by electron beam evaporation at a rate of 2.0 A s-1 in a Sharon electron beam evaporator. Finally, the photoresist was removed in solvent stripper (Remover PG, MicroChem) to pattern the metal mask by lift-off.

TPP collimator fabrication: The collimator was fabricated using a NanoOne TPP printer from UpNano GmbH, a printer equipped with a femtosecond fiber laser operating at 780 nm capable of achieving up to 1000 mW of time-averaged optical power with pulse length of 90 fs. First, the fiber was stripped and cleaved using an automated fiber cleaver (CT50 from Fujikura), followed by mounting on the fiber and ferrule holder available from UpNano. The collimator was made of IP-S (Nanoscribe GmbH), a resin with refractive index of 1.5 at 1550 nm that known for its smooth surfaces which is often used for micro-optics. Printing was done using the 40x objective and adaptive resolution, a method where the outline of a shape is printed with fine details while the inside bulk is printed more with a more defocused beam at higher power so as to increase printing throughput. The printing parameters used to expose the resin were 100 nm of in-plane hatching distance and 300 nm of out-of-plane slicing distance, with a scan speed of 100 mm/s and an optical averaged power of 10 mW for the outline, and 1 μm hatching distance, 0.5 μm slicing distance, 150 mm/s at an exposure power of 20 mW for the bulk. To finish, the collimator was washed in 2 baths of PGMEA (10 min each), and two more baths of IPA (2 min each).

Metalens characterization: The metalens sample was positioned on a three-axis translation stage and illuminated from the substrate side with a collimated laser beam (Keyseight Agilent B163B). The focal spot produced by the metalens was magnified using the telescope assembly composed by a first lens of 15 mm and a second lens of 75 mm. The magnified image of the focal spot was captured by a thermo-electrically cooled InGaAs detector with 320 × 256 pixels (Xeva-1.7-320, Xenics Infrared Solutions).

Funding

This work was supported by the Agència Valenciana d'Innovació (AVI) through AVI's Promotion of Talent program [grant number INNTA3/2023/22, award number 9738,129, budget line S7062000 (2023 2 S7062 3 1)].

Data availability

Data underlying the results presented in this paper are not publicly available at this time but may be obtained from the authors upon reasonable request.

CRediT authorship contribution statement

David M.G. de la Sacristana: Writing – review & editing, Writing – original draft, Visualization, Validation, Software, Resources, Project administration, Methodology, Investigation, Funding acquisition, Formal analysis, Data curation, Conceptualization. **Luigi Ranno:** Resources, Methodology, Investigation, Conceptualization. **Hung-I Lin:** Resources, Data curation. **Fan Yang:** Supervision, Software, Resources, Methodology, Investigation. **Mario Cortijo:** Software, Resources, Investigation, Data curation. **Javier Martí:** Supervision. **Tian Gu:** Supervision. **Carlos García-Meca:** Writing – original draft, Supervision, Formal analysis. **Juejun Hu:** Writing – original draft, Supervision.

Declaration of competing interest

The authors declare that they have no known competing financial interests or personal relationships that could have appeared to influence the work reported in this paper.

Supplementary materials

Supplementary material associated with this article can be found, in the online version, at doi:10.1016/j.optlaseng.2025.109279.

References

[1] Yu N, et al. Light propagation with phase discontinuities: generalized laws of reflection and refraction. Science (1979) 2011;334(6054):333–7. https://doi.org/10.1126/science.1210713.

[2] Yu N, Capasso F. Flat optics with designer metasurfaces. Nat Mater 2014;13(2):139–50. https://doi.org/10.1038/nmat3839.

[3] Qiu CW, Zhang T, Hu G, Kivshar Y. Quo vadis, metasurfaces? American Chemical Society; 2021. https://doi.org/10.1021/acs.nanolett.1c00828.

[4] Yang F, et al. Reconfigurable parfocal zoom metalens. Adv Opt Mater 2022;10(17). https://doi.org/10.1002/adom.202200721.

[5] Yang F, An S, Shalaginov MY, Zhang H, Hu J, Gu T. Understanding wide field-of-view flat lenses: an analytical solution. Chin Opt Lett 2023;21(2):023601. https://doi.org/10.3788/COL202321.023601.

[6] Zhang Y, et al. Electrically reconfigurable non-volatile metasurface using low-loss optical phase-change material. Nat Nanotechnol 2021;16(6):661–6. https://doi.org/10.1038/s41565-021-00881-9.

[7] Zhang L, et al. Ultra-thin high-efficiency mid-infrared transmissive Huygens meta-optics. Nat Commun 2018;9(1):1481. https://doi.org/10.1038/s41467-018-03831-7.

[8] Kurosawa H, Choi B, Sugimoto Y, Iwanaga M. High-performance metasurface polarizers with extinction ratios exceeding 12000. Opt Express 2017;25(4):4446. https://doi.org/10.1364/OE.25.004446.

[9] Ren H, et al. An achromatic metafiber for focusing and imaging across the entire telecommunication range. Nat Commun 2022;13(1). https://doi.org/10.1038/s41467-022-31902-3.

[10] Yuan Z, Huang S-H, Qiao Z, Wu PC, Chen Y-C. Metasurface-tunable lasing polarizations in a microcavity. Optica 2023;10(2):269. https://doi.org/10.1364/OPTICA.478616.

[11] Udem Th, Holzwarth R, Hänsch TW. Optical frequency metrology. Nature 2002;416(6877):233–7. https://doi.org/10.1038/416233a.

[12] Wieser W, Biedermann BR, Klein T, Eigenwillig CM, Huber R. Multi-megahertz OCT: high quality 3D imaging at 20 million A-scans and 45 GVoxels per second. Opt Express 2010;18(14):14685. https://doi.org/10.1364/OE.18.014685.

[13] Keller U. Recent developments in compact ultrafast lasers. Nature 2003;424(6950):831–8. https://doi.org/10.1038/nature01938.

[14] Kues M, et al. Passively mode-locked laser with an ultra-narrow spectral width. Nat Photon 2017;11(3):159–62. https://doi.org/10.1038/nphoton.2016.271.

[15] Gao B, et al. Generation and categories of solitons in various mode-locked fiber lasers. Optik (Stuttg) 2020;220:165168. https://doi.org/10.1016/j.ijleo.2020.165168.

[16] Haring R, Paschotta M, Aschwanden A, Gini E, Morier-Genoud F, Keller U. High-power passively mode-locked semiconductor lasers. IEEE J Quant Electron 2002;38(9):1268–75. https://doi.org/10.1109/JQE.2002.802111.

[17] Najm MM, et al. Sodium carbonate for generating Q-switched pulses in 1550 nm region. Taylor and Francis Ltd; 2021. https://doi.org/10.1080/01468030.2021.1942334.

[18] Najm MM, Abdullah MN, Almukhtar AA, Hamida BA, Yasin M, Harun SW. 8-HQCdCl2H2O as an organic Q-switcher in erbium laser cavity. Optoelectron Lett 2023;19(11):681–5. https://doi.org/10.1007/s11801-023-3009-x.

[19] Zhang P, et al. Bismuth-doped fiber Q-switcher in erbium-doped fiber laser cavity. Microw Opt Technol Lett 2021;63(8):2214–8. https://doi.org/10.1002/mop.32870.

[20] Zhang P, Dimyati K, Nizamani B, Najm MM, Harun SW. Sequential generation of self-starting diverse operations in all-fiber laser based on thulium-doped fiber saturable absorber. Chin Phys B 2022;31(6). https://doi.org/10.1088/1674-1056/ac3ba9.

[21] Harun SW, Najm MM, Rosol AHA. Ultrafast laser generation using MAX phase material as a mode-locker. In: AIP Conference Proceedings. American Institute of Physics Inc.; May 2023. https://doi.org/10.1063/5.0123307.

[22] Liang Z, et al. >10 GHz femtosecond fiber laser system at 2.0 μm. Opt Lett 2022;47(7):1867. https://doi.org/10.1364/ol.454024.

[23] Song J, et al. Compact low-noise passively mode-locked Er-doped femtosecond all-fiber laser with 268 GHz fundamental repetition rate. Appl Opt 2019;58(7):1733. https://doi.org/10.1364/ao.58.001733.

[24] McFerran JJ, et al. A passively mode-locked fiber laser at 1.54 μm with a fundamental repetition frequency reaching 2 GHz References and links "Coherent optical link over hundreds of metres and hundreds of terahertz with subfemtosecond timing jitter. 2007. https://doi.org/10.1364/OA_License_v1#VOR.

[25] Gao X, et al. Stable 5-GHz fundamental repetition rate passively SESAM mode-locked Er-doped silica fiber lasers. Opt Express 2021;29(6):9021. https://doi.org/10.1364/oe.414779.

[26] Song YF, Zhang H, Tang DY, Shen DY. Polarization rotation vector solitons in a graphene mode-locked fiber laser. 2012. https://doi.org/10.1364/OA_License_v1#VOR.

[27] Wang Y, Wang M. Research progress on all-polarization-maintaining mode-locked fiber lasers. Multidisciplinary Digital Publishing Institute (MDPI); 2025. https://doi.org/10.3390/photonics12040366.

[28] Avazpour M, et al. The use of polarization-imbalanced NOLM to improve the quality of the spectrum compression. Opt Laser Technol 2019;120. https://doi.org/10.1016/j.optlastec.2019.105692.

[29] Wang J, et al. Saturable plasmonic metasurfaces for laser mode locking. Light Sci Appl 2020;9(1):50. https://doi.org/10.1038/s41377-020-0291-2.

[30] Yang J, et al. Photonic crystal fiber metalens. Nanophotonics 2019;8(3):443–9. https://doi.org/10.1515/nanoph-2018-0204.

[31] Cheng H, et al. 5 GHz fundamental repetition rate, wavelength tunable, all-fiber passively mode-locked Yb-fiber laser. Opt Express 2017;25(22):27646. https://doi.org/10.1364/OE.25.027646.

[32] Byun H, et al. Compact, stable 1 GHz femtosecond Er-doped fiber lasers. Appl Opt 2010;49(29):5577. https://doi.org/10.1364/AO.49.005577.

[33] Keller U. Ultrafast lasers. Cham: Springer International Publishing; 2021. https://doi.org/10.1007/978-3-030-82532-4.

[34] Cao S, et al. Two-photon direct laser writing of micro Fabry-Perot cavity on single-mode fiber for refractive index sensing. Opt Express 2022;30(14):25536. https://doi.org/10.1364/OE.464210.

[35] Gissibl T, Thiele S, Herkommer A, Giessen H. Two-photon direct laser writing of ultracompact multi-lens objectives. Nat Photon 2016;10(8):554–60. https://doi.org/10.1038/nphoton.2016.121.

[36] Vanmol K, et al. 3D direct laser writing of microstructured optical fiber tapers on single-mode fibers for mode-field conversion. Opt Express 2020;28(24):36147. https://doi.org/10.1364/OE.409148.

[37] Chandrahalim H, Williams JC, Smith JW, Suelzer JS, Usechak NG. Micromechanically enabled microcavity on optical fiber tips. In: 2021 IEEE Research and Applications of Photonics in Defense Conference (RAPID). IEEE; 2021. p. 1–2. https://doi.org/10.1109/RAPID51799.2021.9521446.

[38] Shalaginov MY, et al. Reconfigurable all-dielectric metalens with diffraction-limited performance. Nat Commun 2021;12(1):1225. https://doi.org/10.1038/s41467-021-21440-9.

[39] Yang F, et al. Design of broadband and wide-field-of-view metalenses. Opt Lett 2021;46(22):5735. https://doi.org/10.1364/OL.439393.

[40] Li J, et al. Kelly sideband suppression and wavelength tuning of a conventional soliton in a Tm-doped hybrid mode-locked fiber laser with an all-fiber Lyot filter. Photon Res 2019;7(2):103. https://doi.org/10.1364/prj.7.000103.

[41] Ou S, et al. GHz-repetition-rate fundamentally mode-locked, isolator-free ring cavity Yb-doped fiber lasers with SESAM mode-locking. Opt Express 2022;30(24):43543. https://doi.org/10.1364/OE.471813.

[42] Hu M, Shen J, Cao Y, Yuan S, Zeng H. Generation of 48 fs, 1 GHz Fundamentally Mode-Locked Pulses Directly from an Yb-doped 'Solid-State Fiber Laser. Photonics 2023;10(2). https://doi.org/10.3390/photonics10020192.

[43] Yan Z, et al. Widely tunable Tm-doped mode-locked all-fiber laser. Sci Rep 2016;6(1):27245. https://doi.org/10.1038/srep27245.